JASA ARTICLE

Spatiotemporal evolution of molar fraction in acoustic-resonance tube filled with He-Ar mixture

Satoshi Sekimoto,[a] Yuji Yamagishi, Takeru Otomo, and Yuki Ueda
Tokyo University of Agriculture and Technology, Koganei, Tokyo 184-8588, Japan

ABSTRACT:
This study proposes a time-evolution method to simulate acoustic gas-mixture separation. The proposed method can calculate the separation process without any arbitrary parameters except for space and time resolutions. The molar-fraction distribution within the system during the separation can be calculated, and the results show that a large molar-fraction gradient occurs in the separation tube, while a distribution also occurs in the resonance tube. Although the simulation results for the case with a high-pressure amplitude diverge from that of the experiment during the process of the separation, the simulation results for the case with a low-pressure amplitude agree well with those of the experiment. © *2024 Acoustical Society of America*. https://doi.org/10.1121/10.0028313

(Received 5 February 2024; revised 9 July 2024; accepted 4 August 2024; published online 30 August 2024)
[Editor: Andi Petculescu] Pages: 1425–1439

I. INTRODUCTION

Acoustic gas-mixture separation was accidentally observed in an experiment that involved two thermoacoustic engines (TAEs) with a He-Xe gas mixture as the working gas performed by a research group at Los Alamos National Laboratory (LANL) in 1999 (Spoor and Swift, 1999). The group provided a detailed explanation of the theory and established equations (Swift and Spoor, 1999; Geller and Swift, 2002a,b) based on linearized thermoacoustic theory and mass-flux transportation driven by the Soret effect (Platten, 2006; Rahman and Saghir, 2014). They also experimentally demonstrated acoustic gas-mixture separation using a He-Ar gas mixture (Spoor and Swift, 2000). In other studies, researchers demonstrated the enrichment of neon isotopes (Geller and Swift, 2004) and continuous separation of a He-Ar gas mixture (Swift and Geller, 2006) via an acoustic method. Additionally, the effect of an axial temperature gradient on the gas-mixture separation was investigated (Geller and Swift, 2009).

According to Swift (1988), Belcher *et al*. presented two characteristics of an ideal working gas for thermoacoustic refrigerators (TARs): a high ratio of specific heat and a low Prandtl number (Belcher *et al*., 1999). They varied the two quantities by mixing binary gases and confirmed that the onset temperature and frequency of their thermoacoustic system varied as theoretically estimated. This result indicates that the gas-mixture properties can be optimized for specific thermoacoustic applications. However, acoustic waves cause the gas-mixture separation, suggesting that the properties of the working gas may change. Therefore, it is important to know in advance the extent to which acoustic gas separation will occur when designing thermoacoustic applications using gas mixtures.

The key to acoustic gas-mixture separation is the combination of an acoustic effect in the axial direction and a thermal effect in the radial direction. Acoustic-wave propagation in a tube induces the compression/expansion of gas and increases/decreases the temperature of gas at the center of the tube owing to adiabatic changes. In contrast, because of the relatively high heat capacity of the tube wall, the temperature of gas near the tube wall is anchored. This difference generates a temperature gradient in the gas in the radial direction and causes molecular movement due to the Soret effect. Molecules near the center of the tube move according to the displacement of the sound wave, whereas molecules near the tube wall hardly move owing to the viscosity. Because the components of the gas and the direction of displacement at the center of the tube change every half-cycle, acoustic gas-mixture separation is performed by repeating the cycle.

Our previous study experimentally revisited acoustic gas-mixture separation (Sekimoto *et al*., 2024). The molar fraction of the gas accumulated in the reservoir tank was measured as a time series using a method involving hammering impact vibration, and the effects of the pressure amplitude and initial molar fraction on the gas-mixture separation were investigated. Further detailed investigations are required for practical application. However, there are several difficulties in experimentally investigating acoustic gas-mixture separation. One of the most significant difficulties is measuring the molar-fraction distribution in the system. The measurement method essentially involves a point measurement at the location where the measurement reservoir is installed, and it is difficult to measure the molar-fraction distribution in the axial direction. Therefore, we used numerical simulations to investigate the acoustic gas-mixture separation.

The LANL research group released a software called Design Environment for Low-amplitude Thermoacoustic Energy Conversion (DELTAEC) (Ward *et al*., 2021), which can calculate the performance of thermoacoustic equipment. This software supports calculations for binary gas mixtures

[a]Email: satoshi-sekimoto@go.tuat.ac.jp

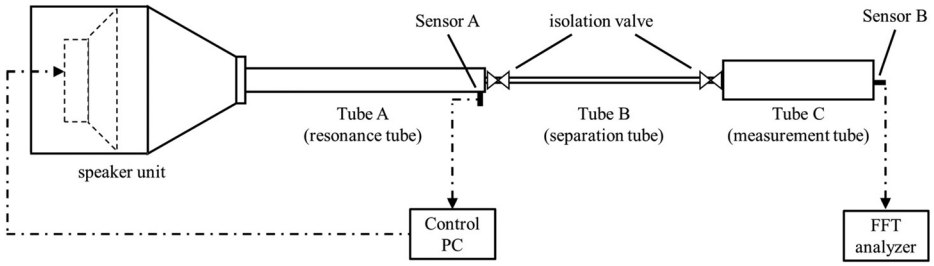

FIG. 1. Schematic of the experimental apparatus.

and can calculate not only acoustic fields but also molar-fraction fields. Calculations are executed using the shooting method, and if all the physical quantities at the starting point ("BEGIN" module in DELTAEC) are not known, users can estimate unknown values by setting known boundary conditions (e.g., the velocity at the end wall is zero because of viscosity). For example, if the molar fraction at the end point reservoir in the saturated state is known from experiments, the molar-fraction distribution in the system can be calculated. In our previous study (Sekimoto *et al.*, 2024), we calculated the acoustic fields and molar-fraction distributions in the separation and measurement tubes under saturated conditions by using DELTAEC. The driving frequency and the molar fraction in the measurement tube were experimentally acquired and used for the boundary conditions of the simulation. However, when the local molar flux is non-zero during separation and its value cannot be estimated, the number of boundary conditions is insufficient, and the field cannot be estimated. In addition, the equations for typical thermoacoustic phenomena are derived via cycle averaging and do not consider the time evolution. Therefore, the temporal variation of the molar-fraction distribution cannot be calculated, and it is difficult to predict how much gas-mixture separation will occur and how long it will take under the given conditions.

To calculate the temporal changes in the molar-fraction distribution, a time-evolutional analysis method is required. This paper proposes a method to simulate the time process of acoustic gas-mixture separation by adding a time-evolution method to the conventional thermoacoustic theory of binary gas mixtures. The paper is organized as follows: Section II describes the physical model of gas-mixture separation. The numerical models used in the simulation are described in Sec. III. This section presents the linearized thermoacoustic equations for the gas mixture, handling of components and boundary conditions of the current system, physical properties of the gas mixture, and proposed time-evolution method. Section IV presents the validation of the current model with experimental results, descriptions of the temporal changes of distributions in gas-mixture separation, and the limitations of the current model. Finally, conclusions are presented in Sec. V.

TABLE I. Dimensions of the tubes in the experimental apparatus.

Name	Description	Length [m]	Radius [mm]
Tube A	Resonance tube	2.00	11.5
Tube B	Separation tube	1.86	2.4
Tube C	Measurement tube	0.148	18.9

II. PHYSICAL MODEL OF GAS-MIXTURE SEPARATION

A. Apparatus

Figure 1 presents a schematic of the experimental apparatus for gas-mixture separation using acoustic waves. The apparatus was primarily composed of a speaker unit, resonance tube (Tube A), separation tube (Tube B), and measurement tube (Tube C). The speaker unit consisted of a loudspeaker (FW168HS, Fostex Ltd., Tokyo, Japan) and was connected to Tube A using a tapered part. The other end of Tube A was connected to Tube B. Tube C was connected to the other end of Tube B. This setup is similar to that used in our previous study (Sekimoto *et al.*, 2024).

Sensors A and B (PD104, Jtect Ltd, Greenville, SC) were used to measure the pressure amplitudes at the ends of Tubes A and C, respectively. The signal from Sensor B was analyzed using a fast Fourier transform analyzer (DS-3000, Onosokki Ltd., Yokohama, Japan) to measure the molar fraction in Tube C. As described in the next subsection, the applied acoustic wave was maintained in resonance in the system and at the target value of the pressure amplitude at Sensor A. Using a data-acquisition system (USB-6363 and BNC-2120, National Instruments Corporation, Austin, TX), the signal from Sensor A was acquired, and the signal to the loudspeaker was generated.

The working gas was a binary mixture of He and Ar. The dimensions of each tube are presented in Table I. The mechanical parameters of the speaker unit, including the Thiele-Small parameters presented in Table II, were applied to the numerical model described in Sec. III.

TABLE II. Mechanical parameters of the speaker unit.

Symbol	Description	Value	Unit
m	Mechanical moving mass	25.9	g
k_0	Mechanical compliance	0.402	mm/N
c	Mechanical resistance	1.18	kg/s
A_s	Projected area of diaphragm	141	cm^2
R	Electrical resistance	4.90	Ω
Bl	Force factor	14.1	T · m
L_{coil}	Inductance of coil	2.10	mH
v_{vessel}	Volume of space behind diaphragm	1.59×10^3	cm^3

https://doi.org/10.1121/10.0028313

B. Experimental procedure

The experimental apparatus aimed to increase the pressure amplitude using resonance. The resonance frequency changes as the separation progresses because the molar-fraction distribution in the system changes. The change in the distribution also affects the voltage amplitude applied to the loudspeaker to achieve the target pressure amplitude at Sensor A. Therefore, the voltage was feedback-controlled according to the signal from Sensor A. In the experiment, the resonance frequency was defined as the frequency at which the pressure amplitude at Sensor A was maximized, and the voltage amplitude to the loudspeaker was fixed at a certain value. At the start of separation, the initial resonance frequency $f_{reso,0}$ is determined by the voltage amplitude at a specific value, and then the first voltage amplitude $V_{reso,0}$ is determined at the driving frequency of $f_{reso,0}$. The resonance frequency $f_{reso,i}$ and voltage amplitude $V_{reso,i}$ are updated every 10 min, where the subscript i denotes the i-th updated value. Based on the results of preliminary experiments, we chose the second resonance frequency as a driving frequency rather than the first resonance frequency due to a better gas-separation capability (see Appendix A).

III. NUMERICAL MODEL FOR TIME-EVOLUTIONAL ANALYSIS OF GAS-MIXTURE SEPARATION

A. Linearized thermoacoustic equations for gas mixture

Geller and Swift (2002a) derived the following one-dimensional spatial linearized equations based on continuity, momentum, thermal transportation, and molar-fraction equations:

$$\frac{dP}{dx} = -\frac{i\omega\rho_m}{(1-\chi_\nu)}U, \tag{1}$$

$$\frac{dU}{dx} = -\frac{i\omega}{\gamma P_m}\{1+(\gamma-1)[B\chi_\nu + C\chi_{\alpha D} + (1-B-C)\chi_{D\alpha}]\}P. \tag{2}$$

These are the equations for the pressure P and velocity U, where i, ω, ρ_m, P_m, and γ represent the imaginary unit, driving angular frequency, mean density, mean pressure, and ratio of specific heat, respectively. $\chi_j (j = \nu, \alpha, \alpha D, D\alpha)$ is a spatially averaged complex function defined as follows:

$$\chi_j = \frac{2J_1(Y_j)}{Y_j J_0(Y_j)}, \tag{3}$$

where

$$Y_j = \frac{(i-1)r}{\delta_j}, \tag{4}$$

and J_α, r, and δ_j represent the Bessel function of the first kind, tube radius, and boundary layer thickness, respectively. The boundary layer thickness is defined as follows:

$$\delta_\nu = \sqrt{\frac{2\nu}{\omega}}, \tag{5}$$

$$\delta_\alpha = \sqrt{\frac{2\alpha}{\omega}}, \tag{6}$$

$$\delta_{\alpha D}^2 = \frac{1}{2}\delta_\alpha^2\left[1+(1+\varepsilon)/L+\sqrt{[1+(1+\varepsilon)/L]^2-4/L}\right], \tag{7}$$

$$\delta_{D\alpha}^2 = \frac{1}{2}\delta_\alpha^2\left[1+(1+\varepsilon)/L-\sqrt{[1+(1+\varepsilon)/L]^2-4/L}\right], \tag{8}$$

where

$$\varepsilon = \frac{\gamma-1}{\gamma}\frac{k_T^2}{n_H(1-n_H)}, \tag{9}$$

$$L = \frac{\alpha}{D_{12}}. \tag{10}$$

Here, ν, α, k_T, n_H, and D_{12} represent the kinematic viscosity, thermal diffusivity, thermal diffusion ratio, molar fraction of the heavier component, and mutual diffusion coefficient, respectively. In Eq. (2), B and C are defined as follows:

$$B = \frac{ie^{-i\theta}\varepsilon}{1-\chi_\nu}\frac{\sigma}{(1-\sigma)(1-\sigma L)-\varepsilon\sigma}\Gamma_c, \tag{11}$$

$$C = \frac{\chi_{D\alpha}(\delta_\alpha^2/\delta_{D\alpha}^2-1)-B[\chi_\nu(\sigma-1)/\sigma+\chi_{D\alpha}(\delta_\alpha^2/\delta_{D\alpha}^2-1)]}{\chi_{D\alpha}(\delta_\alpha^2/\delta_{D\alpha}^2-1)-\chi_{\alpha D}(\delta_\alpha^2/\delta_{\alpha D}^2-1)}. \tag{12}$$

Γ_c is defined as follows:

$$\Gamma_c = \frac{dn_H/dx}{(dn_H/dx)_{sat}}, \tag{13}$$

where

$$(dn_H/dx)_{sat} = \frac{\gamma-1}{\gamma}k_T\frac{|P|}{P_m}\frac{\omega}{|U|}. \tag{14}$$

$(dn_H/dx)_{sat}$ represents the theoretical saturation of the molar-fraction gradient derived from the molar fraction equation, and Γ_c is regarded as a figure of merit for the progress of the separation toward saturation.

It is noteworthy that Eq. (2) does not consider the temperature gradient in the apparatus. It has been reported that when a temperature gradient of approximately 200 K/m is applied, the separation effect is changed by approximately 4%/m (Geller and Swift, 2009). In fact, temperature differences were experimentally observed in the axial direction owing to thermoacoustic heat flow (Merkli and Thomann, 1975) when the pressure amplitude of the acoustic field was relatively high. However, it was experimentally determined that the maximum temperature difference corresponded to

approximately 6 K/m. Assuming this temperature gradient, the molar flux generated by the temperature gradient is approximately 3% of that calculated by Eq. (15). Therefore, we considered that the effect of the temperature gradient is ignorable under the current conditions and used equations without a temperature gradient, which reduced the number of calculations required. The equations that consider a temperature gradient can be found in Geller and Swift (2009).

Geller and Swift (2002a) investigated the mass-flux density equation and derived the following cycle-averaged molar flux for the heavier component $\dot{N}_H$):

$$\frac{\dot{N}_H}{A_{gas}} = \frac{\delta_\alpha}{4r_h}\frac{\gamma-1}{\gamma}\frac{k_T}{R_{univ}T_m}|P||U|(F_{trav}\cos\theta + F_{stand}\sin\theta) + \frac{dn_H}{dx}\left(\frac{\delta_\alpha}{4r_h}\frac{\rho_m|U|^2}{m_{avg}\omega}F_{grad} - \frac{\rho_m}{m_{avg}}D_{12}\right), \tag{15}$$

where r_h, R_{univ}, and θ represent the hydraulic radius, universal gas constant, and phase by which P leads U, respectively. m_{avg} represents the molar average mass, which is defined as

$$m_{avg} = m_H n_H + m_L(1-n_H), \tag{16}$$

where m_H and m_L represent the molar masses of the heavier and lighter gases, respectively. The three F values in Eq. (15) are defined as follows:

$$F_{trav} = -\frac{2r_h}{\delta_\alpha}\mathrm{Re}\left[\frac{G}{1-\widetilde{\chi_\nu}}\right], \tag{17}$$

$$F_{stand} = \frac{2r_h}{\delta_\alpha}\mathrm{Im}\left[\frac{G}{1-\widetilde{\chi_\nu}}\right], \tag{18}$$

$$F_{grad} = -\frac{2r_h}{\delta_\alpha}\frac{1}{|1-\chi_\nu|^2}\frac{\sigma}{(1-\sigma)(1-\sigma L)-\varepsilon\sigma} \times \mathrm{Im}\left[\frac{1-\sigma}{\sigma S}\chi_\nu\left(\frac{\delta_\alpha^2-\delta_{\alpha D}^2}{\delta_\nu^2+\delta_{\alpha D}^2}\chi_{\alpha D} - \frac{\delta_\alpha^2-\delta_{D\alpha}^2}{\delta_\nu^2+\delta_{D\alpha}^2}\chi_{D\alpha} + \frac{(1+\sigma)LQ}{M}\widetilde{\chi_\nu} + S\right) + \varepsilon G\right]. \tag{19}$$

S, Q, M, and G are defined as follows:

$$S = \left(\frac{\delta_\alpha^2}{\delta_{D\alpha}^2}-1\right)\chi_{D\alpha} - \left(\frac{\delta_\alpha^2}{\delta_{\alpha D}^2}-1\right)\chi_{\alpha D}, \tag{20}$$

$$Q = \frac{\delta_{\alpha D}^2-\delta_{D\alpha}^2}{\delta_\alpha^2}, \tag{21}$$

$$M = (1+\sigma)(1+\sigma L)+\varepsilon\sigma, \tag{22}$$

$$G = \frac{\sigma LQ}{MS}\chi_{\alpha D}\chi_{D\alpha} + \frac{\widetilde{\chi_\nu}}{S}\left(\frac{\chi_{\alpha D}}{1+\delta_\nu^2/\delta_{D\alpha}^2} - \frac{\chi_{D\alpha}}{1+\delta_\nu^2/\delta_{\alpha D}^2}\right). \tag{23}$$

Here, σ represents the Prandtl number, and the notation $\widetilde{\ }$ denotes the complex conjugate.

If $\dot{N}_H$ in Eq. (15) is non-zero in the apparatus, the separation is in progress, and when $\dot{N}_H$ becomes zero at all locations, the separation is considered to have converged. Therefore, $\dot{N}_H$ plays an important role in the temporal evolution of the molar-fraction distribution. Note that Eq. (15) was derived by cycle-averaging the second-order term of the molar flux; hence, $\dot{N}_H$ is different from the instantaneous time derivative of a physical quantity. As described in Sec. III D, $\dot{N}_H$ is treated as a time differential value for the temporal evolution of the molar-fraction distribution.

B. System components and boundary conditions

As mentioned in Sec. II B, the resonance frequency and the voltage amplitude are updated every 10 min, and the loudspeaker is driven with these parameters until the next update. This implies that the boundary condition of the acoustic field is determined not by the acoustic requirements but by the electrical requirements. Therefore, an acoustic-electrical model of the loudspeaker is required.

Kurai *et al.* (2024) obtained the following equation by combining the equations of motion that consider the acoustic, electrical, and mechanical forces on the loudspeaker diaphragm. This equation indicates the relationship between the voltage V and current I applied to the loudspeaker and the acoustic fields P_{dia} and U_{dia} generated on the diaphragm surface,

$$V = \frac{U_{dia}}{Bl}\left[Z_e\left(\frac{P_{dia}}{U_{dia}}A_{dia} + Z_{mec}\frac{A_{tube}}{A_{dia}}\right) + (Bl)^2\frac{A_{tube}}{A_{dia}}\right], \tag{24}$$

$$I = \frac{V}{Z_e + \dfrac{(Bl)^2}{Z_{mec}}}. \tag{25}$$

Here,

$$Z_e = R + i\omega L, \tag{26}$$

$$Z_{mec} = c + i\{\omega m - (k+k_g)/\omega\}. \tag{27}$$

A_{tube} and A_{dia} represent the cross-sectional areas of the tube connected to the loudspeaker front and the projected area of the diaphragm, respectively. k_g represents the stiffness of the volume of gas sealed behind the diaphragm and is defined as follows (Tijani *et al.*, 2002):

$$k_g = \gamma_{dia}\frac{P_m}{v_{vessel}}A_{dia}^2, \tag{28}$$

where γ_{dia} denotes the specific heat ratio of the gas in front of the diaphragm. In contrast to reality, it is impossible to determine the acoustic field at the diaphragm from the electrical input using Eqs. (24) and (25). To simulate the experiments, it is necessary to search for an acoustic field that satisfies the electrical input while satisfying the acoustic boundary conditions. In this simulation, the acoustic field inside the tapered tube between the loudspeaker diaphragm and Tube A is considered. However, calculating the partial

https://doi.org/10.1121/10.0028313

differential equations shown in Eqs. (1) and (2) was difficult while considering the molar-fraction gradient of the tapered pipe and the conservation of the molar amount in the entire system. As shown in Fig. 5, a relatively small molar-fraction gradient was generated in Tube A, which has a larger diameter than Tube B, and the tapered pipe has a larger diameter than Tube A. Therefore, we assumed a constant molar fraction in the tapered pipe. The pressure and velocity at the inlet of the tapered pipe were given for P_{dia} and U_{dia} in Eq. (24).

Preliminary simulations indicated that it is important to consider the local energy loss (minor loss) at the rapid tube-area expansion/contraction in the experimental equipment. Ueda *et al.* proposed the following minor-loss model (Ueda *et al.*, 2020):

$$\Delta W = \frac{2}{3\pi}\rho_m K_{loss}|U_{small}|^3 A_{small}, \tag{29}$$

$$K_{loss} = \frac{1}{2}\left(1-\frac{A_{small}}{A_{large}}\right)^2 + \frac{1}{4}\left(1-\frac{A_{small}}{A_{large}}\right)^{3/4}, \tag{30}$$

where the subscripts "small" and "large" denote the values for pipes with small and large cross-sectional areas, respectively. Note that the value of a pipe with a smaller cross-sectional area is always used to calculate the minor loss, regardless of rapid tube-area expansion or contraction.

The acoustic field was estimated using the current molar-fraction distribution and two boundary conditions. The condition in which the velocity at the right end of Tube C is zero is a common boundary condition. When the loudspeaker input voltage was adjusted, the second boundary condition was used to ensure that the pressure amplitude at Sensor A was the target value. At other times, the second boundary condition is the loudspeaker input voltage amplitude, which is calculated using Eqs. (24) and (25), and matches the voltage amplitude determined during the adjustment.

C. Physical properties of gas mixture

Simulations of the gas-separation process require gas-mixture physical properties, which depend on not only the mean pressure and temperature but also the local molar fraction. This paper presents a method for estimating the physical properties of a gas mixture using values calculated with the partial pressure of each gas in advance.

Hereinafter, the subscripts H and L denote the values of the heavier and lighter components of the gas, respectively, and the subscript mix denotes the values of a gas mixture unless otherwise noted. The partial pressure and mass fractions were calculated as follows using the molar fractions n_L and n_H ($n_H + n_L = 1$):

$$P_{mH} = P_m\, n_H, \quad P_{mL} = P_m - P_{mH}, \tag{31}$$

$$X_H = \frac{m_H\, n_H}{m_H\, n_H + m_L\, n_L}, \quad X_L = 1 - X_H. \tag{32}$$

In this study, approximate polynomials related to temperature and pressure were created for five physical properties: ρ_m, γ, constant-pressure specific heat c_p, viscosity μ, and thermal conductivity κ. The physical-property values of each component were calculated using Tm, P_{mH}, or P_{mL}.

The density of the gas mixture was obtained by simply adding the densities of each component calculated using the partial pressure, as follows:

$$\rho_{m,mix} = \rho_{m,H} + \rho_{m,L}. \tag{33}$$

The constant-pressure specific heat, constant-volume specific heat, and the specific heat ratio were calculated using the mass fractions X_L and X_H as follows:

$$c_{p,mix} = c_{p,H}\, X_H + c_{p,L}\, X_L, \tag{34}$$

$$c_{v,mix} = c_{v,H}\, X_H + c_{v,L}\, X_L = \frac{c_{p,H} X_H}{\gamma_H} + \frac{c_{p,L} X_L}{\gamma_L}, \tag{35}$$

$$\gamma_{mix} = \frac{c_{p,mix}}{c_{v,mix}}. \tag{36}$$

The viscosity of the gas mixture was obtained as a weighted average using the molar fraction and the gas-mixture viscosity parameters ϕ_{HL}, ϕ_{LH} (Oe, 1985),

$$\mu_{mix} = \frac{n_H}{n_H + n_L\,\phi_{HL}}\mu_H + \frac{n_L}{n_L + n_H\,\phi_{LH}}\mu_L. \tag{37}$$

Here,

$$\phi_{HL} = \frac{\left[1+\left(\frac{\mu_H}{\mu_L}\right)^{1/2}\left(\frac{M_{WL}}{M_{WH}}\right)^{1/4}\right]^2}{\left[8\left(1+\frac{M_{WH}}{M_{WL}}\right)\right]^{1/2}},$$

$$\phi_{LH} = \phi_{HL}\frac{\mu_L}{\mu_H}\frac{M_{WH}}{M_{WL}}. \tag{38}$$

The thermal conductivity of the gas mixture was obtained as a weighted average of the molar fraction and thermal conductivity parameters A_{HL} and A_{LH},

$$\kappa_{mix} = \frac{n_H}{n_H + n_L\, A_{HL}}\kappa_H + \frac{n_L}{n_L + n_H\, A_{LH}}\kappa_L. \tag{39}$$

Here,

$$A_{HL} = \frac{1}{4}\left\{1+\left[\frac{\mu_H}{\mu_L}\left(\frac{M_{WL}}{M_{WH}}\right)^{3/4}\frac{T_m+S_H}{T_m+S_L}\right]^{1/2}\right\}^2\frac{T_m+S_{mix}}{T_m+S_H}, \tag{40}$$

$$A_{HL} = \frac{1}{4}\left\{1+\left[\frac{\mu_L}{\mu_H}\left(\frac{M_{WH}}{M_{WL}}\right)^{3/4}\frac{T_m+S_L}{T_m+S_H}\right]^{1/2}\right\}^2\frac{T_m+S_{mix}}{T_m+S_L}. \tag{41}$$

In these equations, S is the Sutherland constant, which is determined using the boiling point T_b of each gas according

to Vogel's rule (Vogel, 1914). The coefficient C_s for C_{mix} is normally 1; however, 0.733 is applied for highly polar gases. Because both components of the gas mixture—He and Ar—are nonpolar molecules, $C_s = 1$ is applied (Lindsay and Bromley, 1950),

$$S_H = 1.5T_{bH}, \quad S_L = 1.5T_{bL}, \quad S_{mix} = C_s(S_H S_L)^{1/2}. \tag{42}$$

Despite the previous explanation, Lindsay and Bromley (1950) reported that H, D, and He do not follow Vogel's rule and that the Sutherland constant of He is 79 K. Therefore, $S_L = 79$ was applied in our simulation.

D_{12} is the mutual diffusion coefficient, which was determined using the method reported by Marrero and Mason (1972),

$$D_{12} = \frac{1}{P_{m,atm}^2}\exp(\ln A + s\ln T_m - \ln[\ln(\phi_0/kT_m)]^2 - S/T_m - S'/T_m^2). \tag{43}$$

Here, k is the Boltzmann constant, and the other coefficients are empirical constants. In the case of He-Ar, $A = 15.21 \times 10^{-3}$, $s = 1.552$, $\phi_0/k = 0.41 \times 10^8$, $S = 1.71$, and $S' = 0.0$.

k_T represents the thermal diffusion ratio, which determines the driving force of the Soret effect. Atkins *et al.* (1939) experimentally investigated the thermal diffusion ratios of noble gas mixtures and reported the following approximate equations for He-Ar mixtures:

$$k_T = 0.65 * \frac{2.5(0.286 * n_H + 0.244 * (1 - n_H))}{2.14 + 1.879 * \frac{n_H}{1 - n_H} + 0.448 * \frac{1 - n_H}{n_H}}. \tag{44}$$

For gas mixtures other than noble gases, the technical report of Leuenberger *et al.* is helpful (Leuenberger and Lang, 2002).

D. Time-evolution simulation for gas-mixture separation

Ordinary linear thermoacoustic theory is expressed as spatial partial differential equations and does not consider time evolution. The molar flux equation shown in Eq. (15) is related to temporal changes, and we propose the time evolution of the molar-fraction distribution by combining this equation with the acoustic-field equations. Figure 2 shows a flow chart of the proposed time-evolution method.

The initial state was assumed to have the same initial molar fraction at all locations. This assumption implies that $dn_H/dx = 0$ and that Γ_c of Eq. (13) becomes zero; therefore, the simultaneous differential equations of Eqs. (1) and (2) can be solved analytically. Hence, the initial acoustic field that satisfies the boundary conditions can be easily calculated. As shown in Fig. 1, this calculation considers the loudspeaker, tapered tube between the loudspeaker and tube A, and tubes A, B, and C as thermoacoustic elements. Additionally, it considers the spatial evolution of the acoustic field using the transfer matrix (Ueda and Kato, 2008) of each element, which is expressed as $\mathcal{M}$ in Fig. 2. Similar to the experimental procedure, we first determined the driving frequency by searching for the frequency that would yield the maximum pressure amplitude using a temporary voltage (2 V in the current calculation). The driving voltage of the loudspeaker was determined to achieve the target pressure amplitude.

After the gas-mixture separation begins, a molar-fraction distribution is generated and dn_H/dx may become non-zero at all locations. Because the tapered tube between the loudspeaker and tube A had an even larger radius than tube A, which had the largest radius among the three tubes, we assumed that the molar fraction in the tapered tube was constant; that is, $dn_H/dx = 0$. When $dn_H/dx \neq 0$, Γ_c of Eq. (13) is not zero, and we must evaluate $(dn_H/dx)_{sat}$. Then, B in Eq. (11) is calculated, and the simultaneous differential Eqs. (1) and (2) are solved. However, $(dn_H/dx)_{sat}$ requires the magnitudes of P and U; thus, these equations cannot be solved explicitly and require convergence calculations.

Once the acoustic field is determined, $\dot{N}_H$ can be calculated using the current molar-fraction distribution as shown in Eq. (15). The molar fraction at each point is updated by considering the inflow from the upstream side of the inspection volume (left side of Fig. 1) and the outflow from the downstream side (right side of Fig. 1). Assuming an ideal gas, the total number of molecules in the inspection volume N_{ALL} is determined using the inspection volume from V_{insp} as follows:

$$N_{ALL} = \frac{P_m V_{insp}}{R_{univ} T_m}. \tag{45}$$

Considering that the molar flux from the left side to the right side Fig. 1 is positive, the amount of change in the heavier component of the inspection volume ΔN_H at the time update interval Δt is

$$\Delta N_H = (\dot{N}_{H,left} - \dot{N}_{H,right})\,\Delta t, \tag{46}$$

where $\dot{N}_{H,left}$ and $\dot{N}_{H,left}$ denote the molar fluxes on the left and right sides of the inspection volume, respectively. Therefore, the change in the molar fraction is given as

$$\Delta n_H = \frac{\Delta N_H}{N_{ALL}}. \tag{47}$$

This method is an explicit time-evolution method, and the values diverge for large Δt as in typical explicit methods for computational fluid dynamics. Although it is possible to define certain conditions, such as the Courant–Friedrichs– Lewy condition of the advection equation, this condition has not yet been derived, and Δt used in the

https://doi.org/10.1121/10.0028313

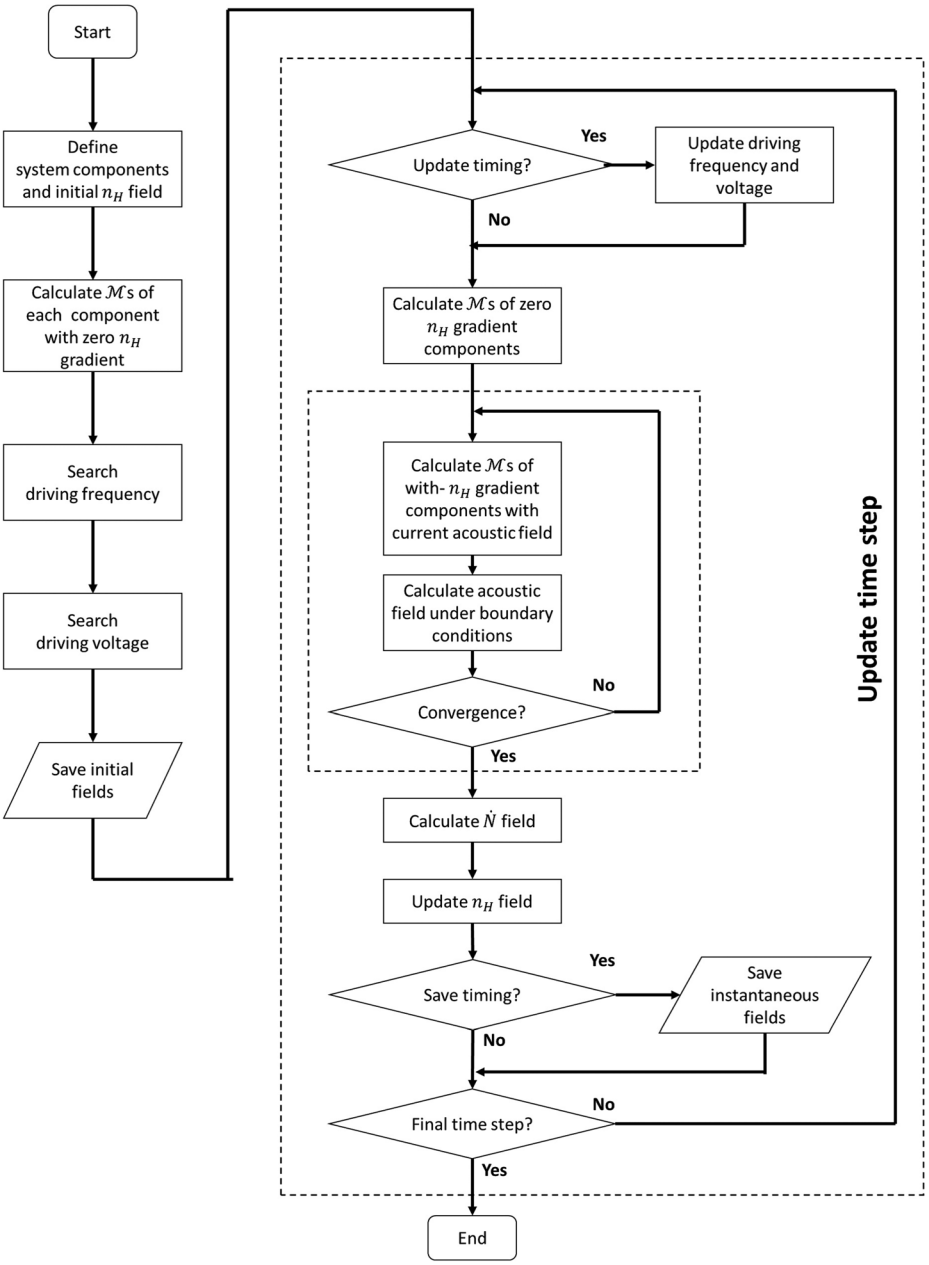

FIG. 2. Flowchart of time-evolution simulation for acoustic gas-mixture separation.

calculation was determined "empirically," as explained later.

Considering the convergence study in Appendix B, the spatial resolution Δx was set to 0.01 m. The convergence study results also indicate that the temporal resolution Δt does not affect the calculation results. Therefore, under $\Delta x = 0.01$ m, Δt was tentatively determined, and a time evolution calculation was performed for 5000 steps. Δt was made smaller when the calculation diverged and Δt was made larger when the calculation was completed. This is the "empirical" method used to determine Δt. Adopting the largest possible Δt with which the calculation does not diverge reduces the calculation time. $\Delta t = 0.1$ s (equivalent to approximately 16 cycles) was selected in the case of a pressure amplitude of 3 kPa.

IV. RESULTS AND DISCUSSION

A. Comparison of computational and experimental results

Figure 3 shows comparisons of temporal changes of state parameters for the gas-mixture separation between the experiment and simulation. The driving frequency was approximately 160 Hz during separation, and the difference between driving frequencies in the experiment and calculation was approximately 2% as shown in Fig. 3(a). The driving voltage of the loudspeaker was adjusted such that the pressure amplitude at Sensor A was at the target value (3000 Pa), and the maximum error in the pressure amplitude during separation was 0.7% in the experiment and 0.04% in the calculation, as shown in Fig. 3(b).

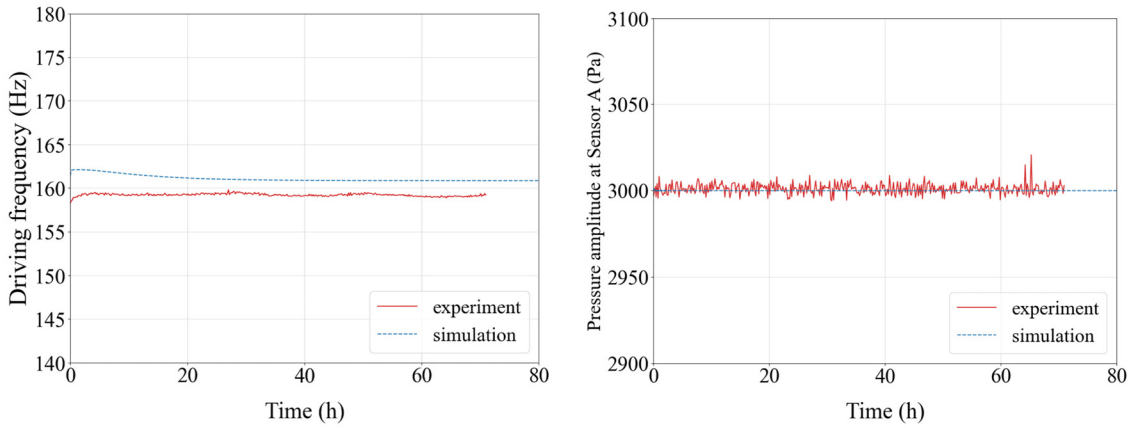

(a) Driving frequency (b) Pressure at Sensor A

FIG. 3. (Color online) Comparison of temporal changes of state parameters for the gas-mixture separation between the experiment and simulation.

Here, the differences in the driving frequency between experiments and simulations are discussed. As shown in the convergence study in Appendix B, the spatial resolution used in the simulation affects the driving frequency, which increases at lower resolutions. Additionally, several differences exist between the current simulation model and the experiment. The first difference is the initial molar-fraction distribution in the apparatus. In the current simulation, the initial molar fraction in Tube C was assumed to be uniformly distributed throughout the apparatus at the start of separation. As performed in the previous study (Sekimoto *et al.*, 2024), force stirring was executed to make a gas mixture using the acoustic wave of the first resonance frequency in Tube A for approximately 1 day before the start of the experiment. However, it is possible that a uniform distribution was not achieved for the initial state of the experiment. The second difference is the volume behind the loudspeaker diaphragm. This volume was used to determine the stiffness of the gas in the acoustic-electrical model of the loudspeaker. The current simulation did not consider the presence of a gas mixture contained in this volume, and the calculation of the specific heat ratio γ_{dia} in Eq. (28) used the molar fraction in front of the diaphragm. However, under real-world conditions, the front and back of the diaphragm are not completely separated, and the mixed gas may move, which is not considered in the calculation.

Figure 4 shows a comparison of the computational and experimental results for the time-dependent molar fraction of He n_{He} in Tube C. Gas separation was conducted under the condition that the initial molar fraction $n_{0,He}$ was 0.506, and the driving frequency corresponded to the second resonance frequency. In the experiments, there was a maximum error of 1 K in the temperature and a maximum error of 1.25 Hz in resonance frequency measurement using fast Fourier transform (FFT), corresponding to a maximum error of 0.3% in the molar fraction. The numerical calculations agree well with the experimental results, validating simulations.

B. Temporal changes of distributions in gas mixture separation

Figure 5 shows the temporal changes in the distributions of the molar fraction of He, n_{He}, for the case depicted in Fig. 4. The location 0 on the plot is the junction of Tube A and Tube B, and this plot includes Tube A (–2.0 to 0.0 m), Tube B (0.0 to 1.86 m), and Tube C (1.86 to 2.0 m). Note that the symbols are provided for visual guidance and do not represent the calculation points. The distribution near the junction of Tubes A and B ($X = 0$) becomes saturated after approximately 1 h. The molar fraction near Tube C ($X = 1.86$) increases over time, and a large molar-fraction gradient is generated along Tube B. It should be noted that the molar-fraction distribution is generated not only in Tube B but also in Tube A, which has a larger radius than Tube B. The pressure amplitude of 3 kPa is the value typically used in TAEs and TARs. As mentioned in the Introduction, when employing a gas mixture whose physical properties are

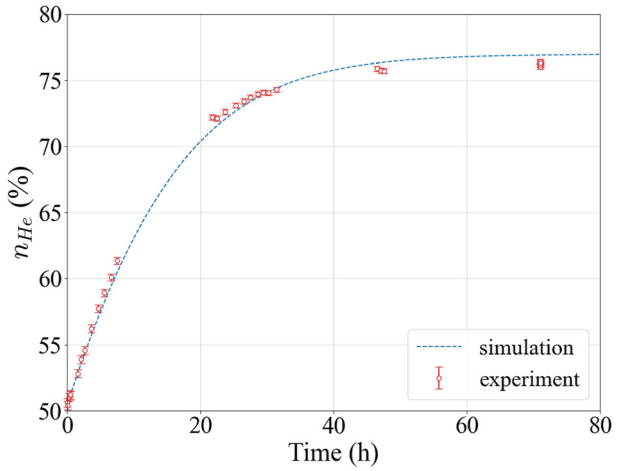

FIG. 4. (Color online) Comparison of experimental and simulation results for the time-dependent molar fraction of He n_{He} in Tube C. Gas separation was conducted under the condition that the initial molar fraction $n_{0,He}$ was 0.506, the pressure amplitude at Sensor A p_A was 3.0 kPa, and the driving frequency corresponded to the second resonance frequency.

https://doi.org/10.1121/10.0028313

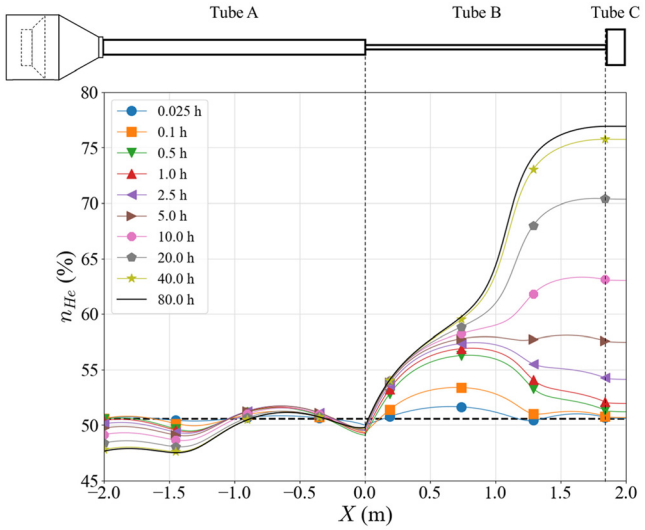

FIG. 5. (Color online) Temporal changes in the distributions of the molar fraction of He n_{He}. This plot includes Tube A (–2.0 to 0.0 m), Tube B (0.0 to 1.86 m), and Tube C (1.86 to 2.0 m). Note that the symbols are provided for visual guidance and do not represent the calculation points.

adjusted to improve performance, users should be aware that gas separation may occur with continued operation and that the physical properties may change.

Figure 6 shows the temporal changes in the distribution of the acoustic field (pressure amplitude, velocity amplitude, and phase difference between pressure and velocity) during separation. The acoustic fields in Tube B change as the separation progresses, whereas the distribution in Tube A hardly changes. This is because the molar-fraction difference in Tube B increases as the separation progresses, and the physical properties of the gas mixture change both spatially and temporally. For example, in the final state, the speed of sound in Tube B changes by 425–570 m/s, while that in Tube A changes by 418–430 m/s.

Figure 7 shows the temporal changes in the distributions of the molar flux of He $\dot{N}_{He}$. There are considerable differences in $\dot{N}_{He}$ depending on the location immediately after the start of gas-mixture separation, and the distribution becomes flat over time. This is because the large initial difference in $\dot{N}_{He}$ generates a local molar-fraction gradient that cancels the excessive difference. Although the distribution of $\dot{N}_{He}$ is flat, the value of $\dot{N}_{He}$ is nonzero; thus, molecules continue to be transported from the speaker unit to Tube C. The value of $\dot{N}_{He}$ approaches zero as the gas-mixture separation progresses, and the separation stops when the value reaches zero.

C. Efficiency of thermoacoustic gas-mixture separation

Geller and Swift (2002b) defined the efficiency of thermoacoustic gas-mixture separation as follows:

$$\eta = \frac{d\dot{G}/dx}{-dW/dx}, \tag{48}$$

where G represents the Gibbs free energy, and $d\dot{G}/dx$ represents the rate at which the Gibbs free energy of the gas mixture increases. Geller and Swift (2002b) derived the following equation for the latter:

$$\frac{d\dot{G}}{dx} = \frac{R_{univ}T_m}{n_H(1-n_H)}\frac{dn_H}{dx}\dot{N}_H. \tag{49}$$

Here, W represents the acoustic power, and $-dW/dx$ represents the amount of energy loss, which can be calculated using the acoustic field,

$$\frac{dW}{dx} = \frac{A_{gas}}{2}\left(\mathrm{Re}\left[\frac{dP}{dx}\tilde{U}\right] + \mathrm{Re}\left[\tilde{P}\frac{dU}{dx}\right]\right). \tag{50}$$

Figure 8 shows the temporal changes in the distributions of the efficiency of gas-mixture separation for the case shown in Figs. 4–7. The maximum efficiency in this plot is approximately 0.0014, which agrees with the investigation of Geller and Swift (2002b) near the junction of Tubes A and B ($X = 0$) 1 h after the start of separation. The efficiency is negative around the middle of Tube B at the start of separation because the molar-fraction gradient temporarily becomes locally negative during separation, and the numerator of Eq. (48) becomes negative. In Tube A, the acoustic energy makes little contribution to the gas-mixture separation, with a maximum efficiency of approximately 0.0001.

The temporal changes in the parameters related to efficiency are presented in Fig. 9. In Fig. 9(a), the acoustic-power consumption of Tube A exceeds that of Tube B, and even if the molar-fraction distribution changes owing to separation, the magnitude of the acoustic-power consumption does not change significantly. Simultaneously, Fig. 9(b) shows that dn/dx increases as separation progresses. Compared with the acoustic fields shown in Fig. 6, there is a tendency for dn/dx to increase near the areas where the velocity amplitude is low. This suggests that the separation efficiency may be low in short separation tubes that do not include velocity amplitude nodes, except at the junction between Tubes A and B ($X = 0$). Tube B can generate a larger concentration gradient with less acoustic-power consumption than Tube A, leading to a higher efficiency. As the separation approaches convergence and $\dot{N}_H$ becomes zero, the overall efficiency decreases.

D. Limitations of the current numerical model

In this section, the applicability of the proposed model is discussed. We experimentally observed that the molar fraction in Tube C in the final state decreased in cases of a high pressure amplitude (Sekimoto *et al.*, 2024). Here, we confirmed that this trend could be reproduced using the current method. Figure 10 shows a comparison of the experimental and simulation results for the time-dependent molar fraction of He n_{He} in Tube C for pressure amplitudes selected in our previous study. Note that the results for a pressure amplitude of 3 kPa are the same as those depicted in Fig. 4. As shown in Fig. 4, not only the final state but also

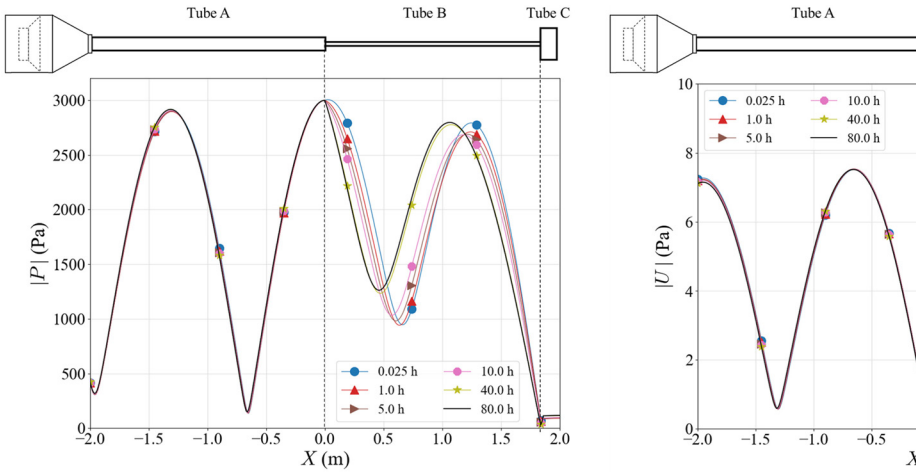

(a) Pressure amplitude $|P|$

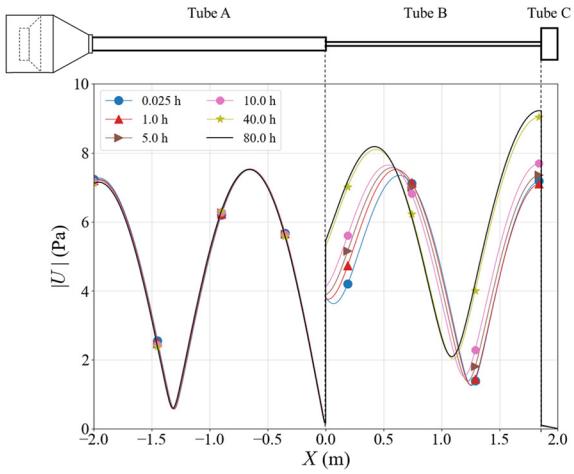

(b) Velocity amplitude $|U|$

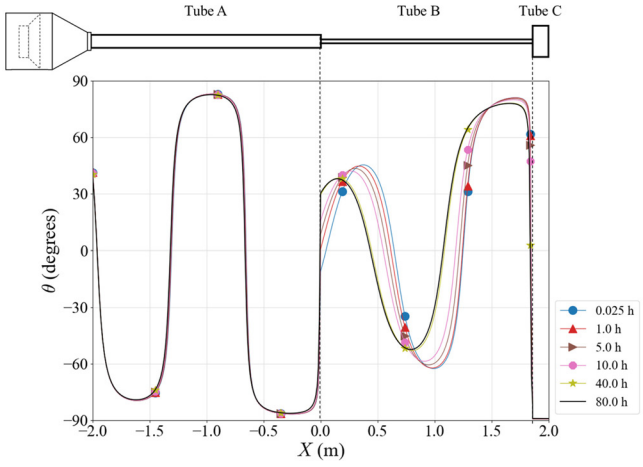

(c) Phase θ

FIG. 6. (Color online) Temporal changes in the acoustic-field distributions. Note that the symbols are provided for visual guidance and do not represent the calculation points.

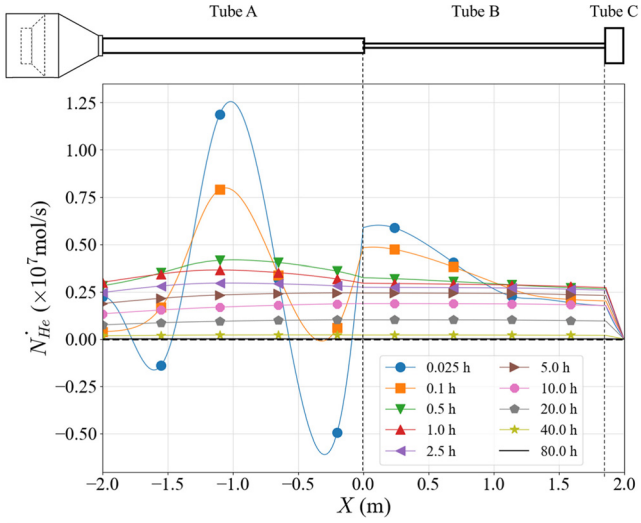

FIG. 7. (Color online) Temporal change in the distributions of the molar flux of He $\dot{N}_{He}$. Note that the symbols are provided for visual guidance and do not represent the calculation points.

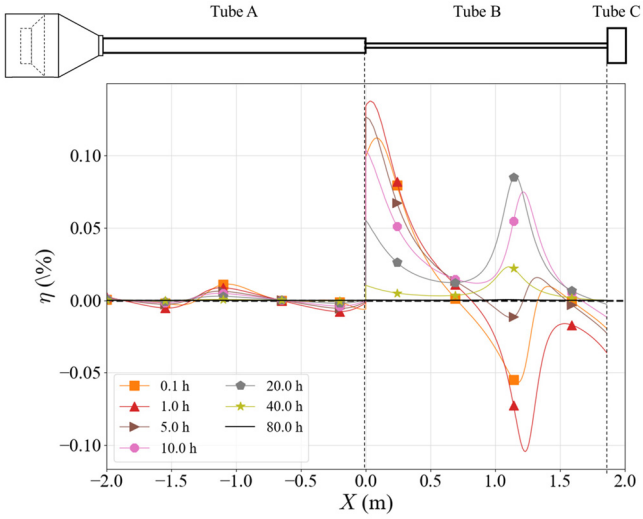

FIG. 8. (Color online) Temporal changes in the distributions of the efficiency of gas-mixture separation. Note that the symbols are provided for visual guidance and do not represent the calculation points.

https://doi.org/10.1121/10.0028313

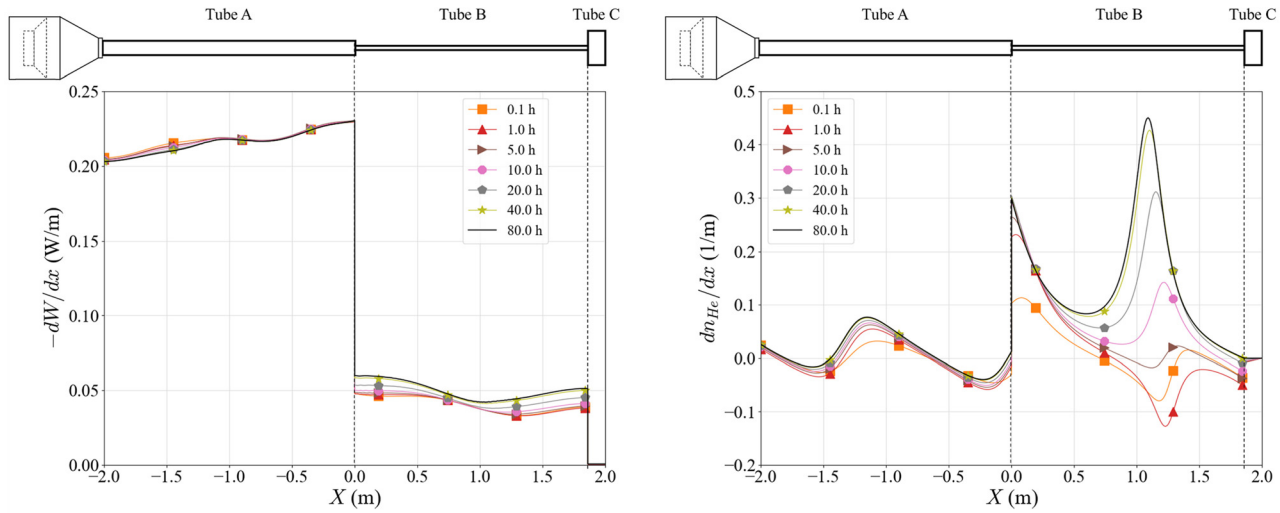

(a) $-dW/dx$ (denominator of Eq. 48) (b) dn_{He}/dx (part of the numerator of Eq. 48)

FIG. 9. (Color online) Temporal changes in the distributions of parameters related to the efficiency. Note that the symbols are provided for visual guidance and do not represent the calculation points.

the progress during the separation agrees well between the experiments and simulations for pressure amplitudes of 1.5 and 3 kPa. Surprisingly, in contrast, for pressure amplitudes of 6 and 9 kPa, the temporal changes of the experiments and simulations agree well with each other up to the middle of the separation process, and then they diverge.

Figure 11 shows a comparison of the experimental and simulation results for the pressure-amplitude dependence of the final molar-fraction increase Δn_{He} as a function of p_B^2 in Tube C. The results indicate that the final molar fraction increases as the pressure amplitude increases in the numerical simulations, whereas the magnitude of this increase decreases at a certain point in the experiments.

Although the cause of the difference between the experimental and computational results is still to be discussed, we consider the turbulence (Ohmi and Iguchi, 1982) generated as the separation progresses to be one of the reasons. The current simulation model is based on linear thermoacoustic theory, and it is assumed that the flow field is always laminar even when a high pressure amplitude is applied to the field. Therefore, the difference between the experiments and simulations is caused by the collapse of the laminar-flow assumption during gas-mixture separation. Because the temporal changes in the experiment and simulation were consistent up to the middle of the separation process, as shown in Fig. 10, it is considered that the separation is inhibited at locations where the molar fraction is high, e.g., in Tube B and at the junction between Tubes B and C. Oosterhuis *et al.* (2017) discussed the relationship between turbulence and flow separation in a jet pump and reported that flow separation was reduced in the turbulent regime. This conclusion suggests that the molar flux between Tubes B and C is affected by the flow conditions at the junction. Vortex rings generated at the junction may also affect this system.

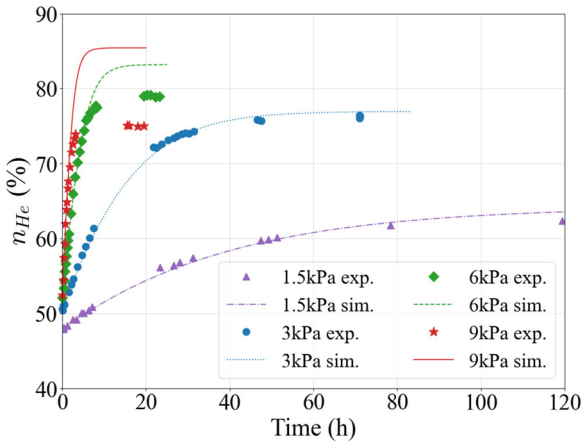

FIG. 10. (Color online) Comparison of experimental and simulation results for the time-dependent molar fraction of He n_{He} in Tube C under various pressure amplitude. The results for 3 kPa are the same as those depicted in Fig. 4.

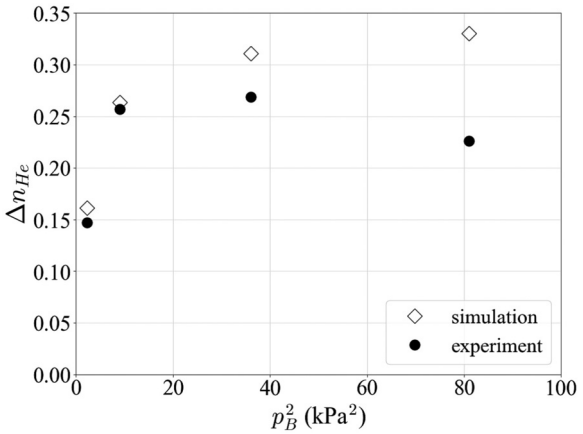

FIG. 11. Comparison of experimental and simulation results for the pressure-amplitude dependence of Δn_{He} as a function of p_B^2 in Tube C.

Oosterhuis *et al*. (2016) visualized the existence of vortex rings from jet pumps. These vortices would cause unexpected mixing and suppress the radial gas movement. In the current apparatus, the junction has a sharp-edged expansion; therefore, changing this part to a tapered shape may suppress the inhibition of separation.

The current model did not reproduce some of the experimental results under high-pressure amplitude (or high-velocity amplitude) conditions. The conditions under which the divergence between the experiment and simulation occurs and the possibility of constructing a model that simulates the divergence state will be explored in future research. A simple approach to clarify the reason for the difference between the experiments and simulations is to increase the number of pressure measurement ports in the apparatus. Although it is possible to install sensor ports in Tubes A and C, it is difficult to install a sensor port on Tube B because of its thin diameter. Increasing the pressure measurement points may enable the discovery of areas where the difference between the experiments and simulations is significant. In the current experiment, the molar fraction in Tube C is measured via the hammering method. The axial distribution of the molar fraction in Tube B may be used to clarify the reason for the difference between the experiment and the calculation; however, it is difficult to measure this distribution. Shoji *et al*. obtained a time-resolved density fluctuation distribution using a phase-shifting Mach–Zehnder interferometer (Shoji *et al*., 2024). Because the molar fraction and density of the mixed gas correspond to one another, this method may be used to obtain the molar-fraction distribution.

V. SUMMARY AND CONCLUSIONS

This paper proposes a method to simulate the time process of acoustic gas-mixture separation by adding a time-evolution method to the conventional thermoacoustic theory of binary gas mixtures. The proposed method can estimate the separation process without any arbitrary parameters except for the space and time resolutions. Additionally, the method can be used to calculate the molar-fraction distribution within the system during separation. The results of this study indicated that a large molar-fraction gradient occurred in the separation tube (Tube B), while some distribution also occurred in the resonance tube (Tube A). The simulation results for a low-pressure amplitude agreed well with the experimental results, whereas the simulation results for a high-pressure amplitude diverged from the experimental results during the separation process.

The proposed computational models and methods can be applied to geometries other than the current experimental apparatus. Selecting appropriate temporal and spatial resolutions enables us to obtain simulation results faster than experiments. In addition, multiple cases can be investigated in parallel on a single workstation. Therefore, rapid optimization of gas-separation devices through numerical calculations will be possible.

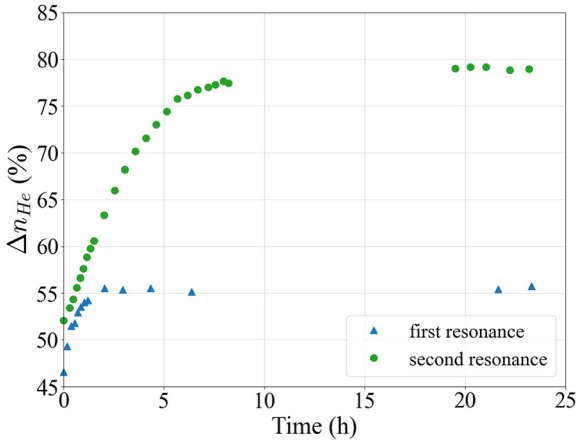

FIG. 12. (Color online) Comparison of experimental results for the time-dependent molar fraction of He n_{He} in Tube C with various driving frequencies. These frequencies were chosen based on the resonance in the current experimental apparatus. The frequencies of the first and second resonances are approximately 55 and 159 Hz, respectively. The results for the secondary resonance are the same as those depicted with green squares in Fig. 10.

ACKNOWLEDGMENTS

This research was funded by the Japan Society for the Promotion of Science (JSPS) through Grants-in-Aid for Scientific Research (KAKENHI) Grant No. JP22H01966. We would like to thank Editage (www.editage.jp) for English language editing.

AUTHOR DECLARATIONS

Conflict of Interest

The authors declare no conflict of interest.

DATA AVAILABILITY

Data are available from the authors upon request.

APPENDIX A: EFFECT OF THE RESONANCE FREQUENCY MODE

Figure 12 shows an experimental comparison of the time-dependent molar fractions of He n_{He} under various driving frequencies. In each case, the initial molar fraction was approximately 50%, and the pressure amplitude at Sensor A was 6.0 kPa. As shown in this figure, operation under the

TABLE III. Calculation cases for the convergence study.

Case #	Δx [m]	ΔT [s]	Calculation time for 10 h gas separation [h]
1 (original)	0.01 (dx_{base})	0.1 (dt_{base})	1.3
2	0.01	0.0025	18.6
3	0.005	0.01 ($d\,t_{base2}$)	9.0
4	0.005	0.005	17.8
5	0.005	0.0025	35.5
6	0.0025	0.0025	86.7
7	0.00125	0.0025	221.7
8	0.02	0.0025	16.8
9	0.04	0.0025	4.5

https://doi.org/10.1121/10.0028313

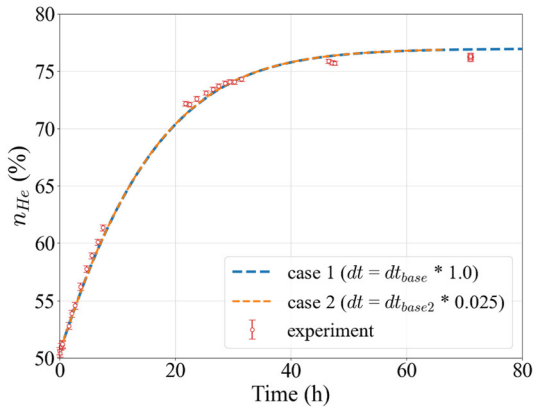

(a) Temporal change of the molar fraction of He in Tube C

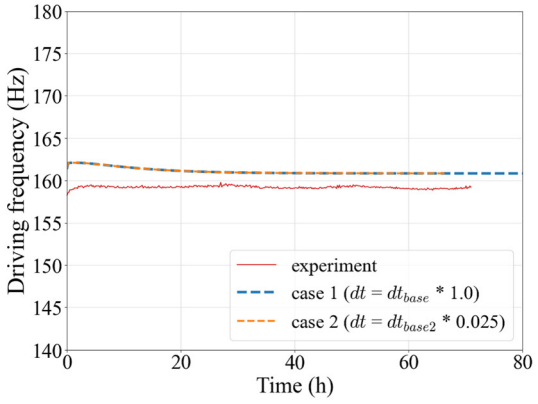

(b) Temporal change of the driving frequency

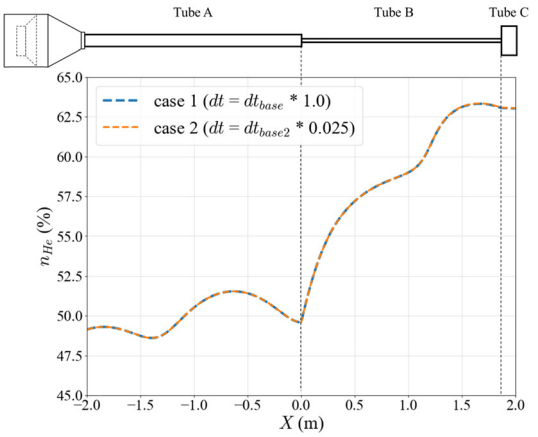

(c) Distributions of the molar fraction of He at 10.0 h after the start of separation

FIG. 13. (Color online) Effect of the temporal resolution ($\Delta x = 0.01$ m).

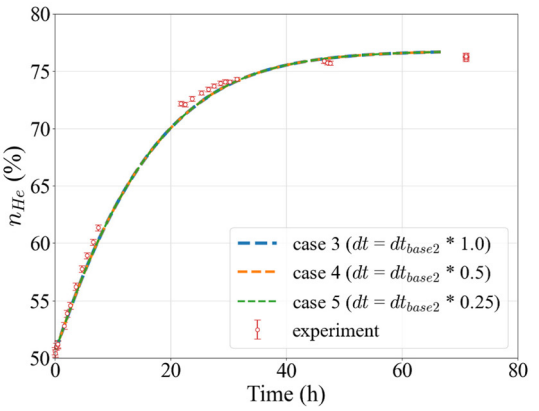

(a) Temporal change of the molar fraction of He in Tube C

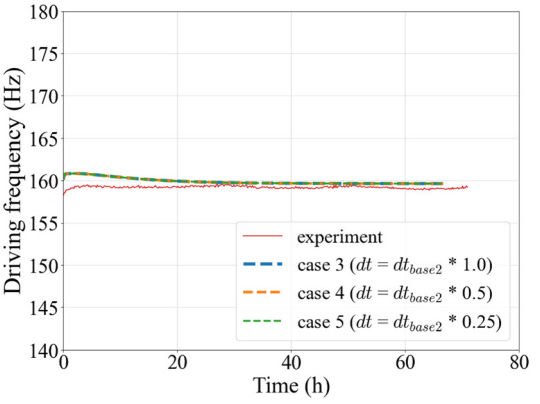

(b) Temporal change of the driving frequency

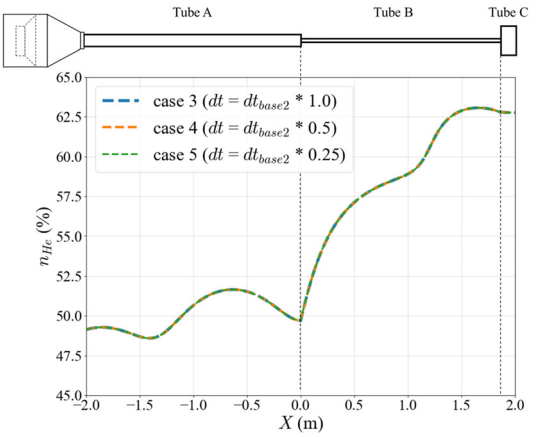

(c) Distributions of the molar fraction of He at 10.0 h after the start of separation

FIG. 14. (Color online) Effect of the temporal resolution Δt ($\Delta x = 0.005$ m).

secondary resonance frequency exhibits a better gas-separation capability than that under the first resonance frequency.

APPENDIX B: CONVERGENCE STUDY

The following cases were selected for the convergence study. All calculations were operated on a CPU (Intel i9-13900 °F 2.00 GHz, Intel, Santa Clara, CA). Because cases with finer spatial or temporal resolutions (such as case 7) required a very long calculation time, the instantaneous values were compared using data 10 h after the start of separation rather than after saturation.

The effect of temporal resolution Δt was investigated for two cases of spatial resolution ($\Delta x = 0.01$ and 0.005 m) in Figs. 13 and 14. The maximum temporal resolutions at

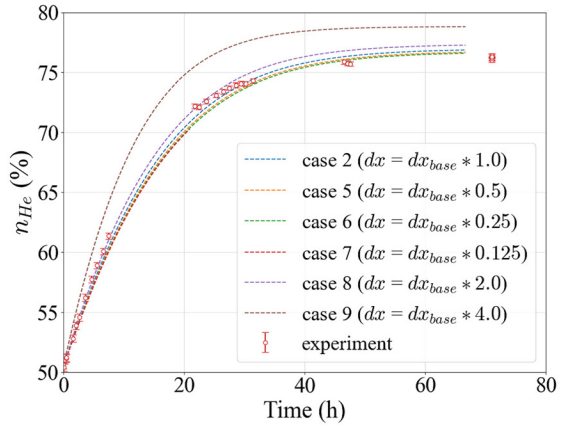

(a) Temporal change of the molar fraction of He in Tube C

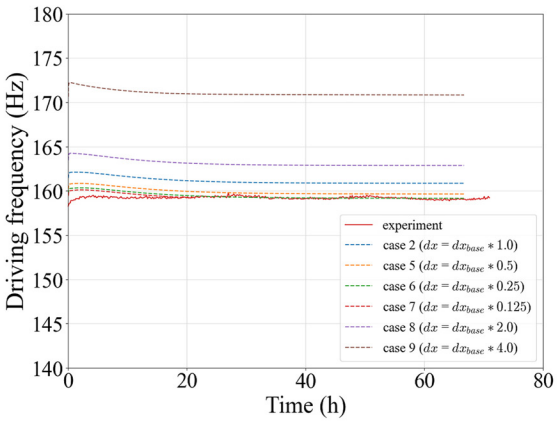

(b) Temporal change of the driving frequency

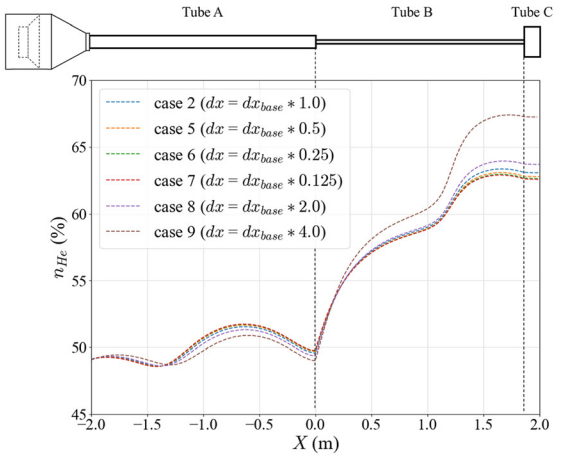

(c) Distributions of the molar fraction of He at 10.0 h after the start of separation

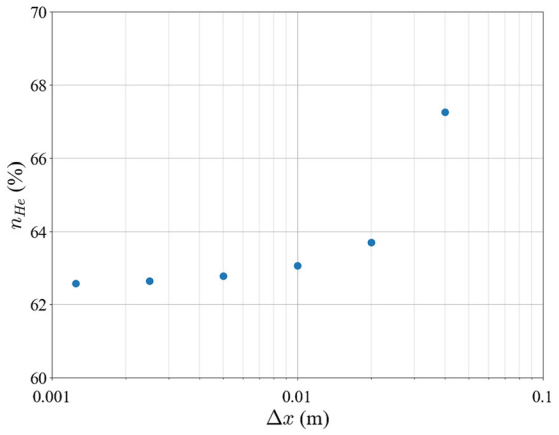

(d) Effect of spatial resolution on the molar fraction of He at 10.0 h in Tube C after the start of separation

FIG. 15. (Color online) Effect of the temporal resolution Δx ($\Delta t = 0.0025$ m).

which the calculation did not diverge for the spatial resolutions of 0.01 and 0.005 m were 0.1 and 0.01 s, respectively. See Table III. Each figure includes three plots: the temporal change of the molar fraction of He in Tube C [Figs. 13(a) and 14(a)], the temporal change of the driving frequency [Figs. 13(b) and 14(b)], and the distributions of the molar fraction of He at 10.0 h after the start of separation [Figs. 13(c) and 14(c)]. As shown in Figs. 13 and 14, the results were consistent across all cases, indicating that the temporal resolution does not affect this gas-separation calculation as long as the calculation does not diverge.

The effect of temporal resolution Δx was investigated for two cases of temporal resolution $\Delta t = 0.0025$ s, which was the maximum temporal resolution at which the calculation did not diverge for the time resolution of 0.00125 m. The results show that a finer spatial resolution lowers the molar fraction of He in Tube B and C and lowers the driving frequency. Figure 15(d) shows the effect of the spatial resolution on the molar fraction of He in Tube C at 10.0 h after the start of separation. The molar fraction converges as the spatial fraction resolution becomes finer, and the difference in the molar fraction is less than 0.6% with d $x \leq 10$. Therefore, considering the calculation time shown in the table, we selected 0.01 m as the spatial resolution for the current calculation.

Atkins, B., Bastick, R., and Ibbs, T. (**1939**). "Thermal diffusion in mixtures of the inert gases," Proc. R. Soc. London. Ser. A. Math. Phys. Sci. **172**(948), 142–158.
Belcher, J. R., Slaton, W. V., Raspet, R., Bass, H. E., and Lightfoot, J. (**1999**). "Working Gases in Thermoacoustic Engines," J. Acoust. Soc. Am. **105**(5), 2677–2684.
Geller, D., and Swift, G. (**2002a**). "Saturation of thermoacoustic mixture separation," J. Acoust. Soc. Am. **111**(4), 1675–1684.
Geller, D., and Swift, G. (**2002b**). "Thermodynamic efficiency of thermoacoustic mixture separation," J. Acoust. Soc. Am. **112**(2), 504–510.
Geller, D., and Swift, G. (**2004**). "Thermoacoustic enrichment of the isotopes of neon," J. Acoust. Soc. Am. **115**(5), 2059–2070.
Geller, D., and Swift, G. (**2009**). "Thermoacoustic mixture separation with an axial temperature gradient," J. Acoust. Soc. Am. **125**(5), 2937–2945.

Kurai, Y., Sekimoto, S., and Ueda, Y. (**2024**). "Measurement of loudspeaker characteristics required for combination with thermoacoustic devices," J. Acoust. Soc. Jpn. **80**(7), 367–373 (in Japanese).
Leuenberger, M., and Lang, C. (**2002**). "Thermal diffusion: An important aspect in studies of static air columns such as firn air, aand dunes and soil air," Technical report (IAEA, Vienna, Austria).
Lindsay, A. L., and Bromley, L. A. (**1950**). "Thermal conductivity of gas mixtures," Ind. Eng. Chem. **42**(8), 1508–1511.
Marrero, T. R., and Mason, E. A. (**1972**). "Gaseous diffusion coefficients," J. Phys. Chem. Reference Data **1**(1), 3–118.
Merkli, P., and Thomann, H. (**1975**). "Thermoacoustic effects in a resonance tube," J. Fluid Mech. **70**(1), 161–177.
Oe, S. (**1985**). *Physical Property Constant Estimation for Engineering Designers* (The Nikkan Kogyo Shimbun, Tokyo) (in Japanese).
Ohmi, M., and Iguchi, M. (**1982**). "Critical Reynolds number in an oscillating pipe flow," Bull. Jpn. Soc. Mech. Eng. **25**(200), 165–172.
Oosterhuis, J. P., Timmer, M. A., Bühler, S., van der Meer, T. H., and Wilcox, D. (**2016**). "On the performance and flow characteristics of jet pumps with multiple orifices," J. Acoust. Soc. Am. **139**(5), 2732–2740.
Oosterhuis, J. P., Verbeek, A. A., Bühler, S., Wilcox, D., and van der Meer, T. H. (**2017**). "Flow separation and turbulence in jet pumps for thermoacoustic applications," Flow. Turbul. Combust. **98**, 311–326.
Platten, J. K. (**2006**). "The Soret effect: A review of recent experimental results," J. Appl. Mech. **73**(5), 5–15.
Rahman, M., and Saghir, M. (**2014**). "Thermodiffusion or Soret effect: Historical review," Int. J. Heat Mass Transfer **73**, 693–705.
Sekimoto, S., Yamagishi, Y., and Ueda, Y. (**2024**). "Revisiting acoustical gas-mixture separation," J. Acoust. Soc. Am. **155**(1), 673–680.
Shoji, E., Maddi, A., Penelet, G., and Biwa, T. (**2024**). "Time-resolved measurement of acoustic density fluctuations using a phase-shifting Mach-Zehnder interferometer," J. Acoust. Soc. Am. **155**(4), 2438–2444.
Spoor, P., and Swift, G. (**1999**). "Mode-locking of acoustic resonators and its application to vibration cancellation in acoustic heat engines," J. Acoust. Soc. Am. **106**(3), 1353–1362.
Spoor, P., and Swift, G. (**2000**). "Thermoacoustic separation of a He-Ar mixture," Phys. Rev. Lett. **85**(8), 1646–1649.
Swift, G. W. (**1988**). "Thermoacoustic engines," J. Acoust. Soc. Am. **84**(4), 1145–1180.
Swift, G., and Geller, D. (**2006**). "Continuous thermoacoustic mixture separation," J. Acoust. Soc. Am. **120**(5), 2648–2657.
Swift, G., and Spoor, P. (**1999**). "Thermal diffusion and mixture separation in the acoustic boundary layer," J. Acoust. Soc. Am. **106**(4), 1794–1800.
Tijani, M., Zeegers, J., and De Waele, A. (**2002**). "A gas-spring system for optimizing loudspeakers in thermoacoustic refrigerators," J. Appl. Phys. **92**(4), 2159–2165.
Ueda, Y., and Kato, C. (**2008**). "Stability analysis of thermally induced spontaneous gas oscillations in straight and looped tubes," J. Acoust. Soc. Am. **124**(2), 851–858.
Ueda, Y., Yonemitsu, S., Ohashi, K., and Okamoto, T. (**2020**). "Measurement and empirical evaluation of acoustic loss in tube with abrupt area change," J. Acoust. Soc. Am. **147**(1), 364–370.
Vogel, H. (**1914**). "Über die viskosität einiger gase und ihre temperaturabhängigkeit bei tiefen temperaturen" ("On the viscosity of some gases and their temperature dependence at low temperatures"), Annalen der Phys. **348**(8), 1235–1272.
Ward, B., Clark, J., and Swift, G. (**2021**)."Design environment for low-amplitude thermoacoustic energy conversion DeltaEC version 6.4b2.7 users guide," https://www.lanl.gov/org/ddste/aldps/materials-physics-applications/quantum/thermoacoustics/computer-codes.php (Last viewed March 6, 2023).